Faceting of equilibrium and metastable nanostructures: a Phase-Field model of surface diffusion tackling realistic shapes

Marco Salvalaglio,[*,†] Rainer Backofen,[‡] Roberto Bergamaschini,[†] Francesco Montalenti,[*,†] and Axel Voigt[‡]

L-NESS and Dipartimento di Scienza dei Materiali,Università di Milano-Bicocca, Via R. Cozzi 55, 20125 Milano, Italy, and Institut für Wissenschaftliches Rechnen, Technische Universität Dresden, 01062 Dresden, Germany

E-mail: marco.salvalaglio@mater.unimib.it; francesco.montalenti@unimib.it

Abstract

Several crystalline structures of present interest are metastable or kinetically-frozen out-of-equilibrium states in the phase space. When the corresponding lifetime is sufficently long, typical equilibrium features such as regular, extended faceting can be observed. However, interpreting the extension of the facets and the overall shape in terms of a simple Wulff analysis is not justified. Here we introduce a convenient general formulation of the anisotropic surface energy density which, combined with a suitable Phase-Field model of surface diffusion, allows for the investigation of the evolution toward equilibrium of three-dimensional nanostructures characterized by arbitrary facets.

[*]To whom correspondence should be addressed

[†]L-NESS and Dipartimento di Scienza dei Materiali,Università di Milano-Bicocca, Via R. Cozzi 55, 20125 Milano, Italy

[‡]Institut für Wissenschaftliches Rechnen, Technische Universität Dresden, 01062 Dresden, Germany

Numerical solution by Finite Element Method allows for efficient simulations even for *strong anisotropy* condition. After illustrating applications yielding equilibrium crystal shapes (corresponding to the Wulff construction), we focus our attention on faceting of structures in long-lived metastable states. The generality and numerical robustness of the approach is proved by few applications to crystalline systems of utmost importance (quantum dots, quantum wires, patterned substrates) in present materials science.

Introduction

The investigation of crystal morphologies is an interdisciplinary topic which plays an important role in the understanding of growth and processing of advanced crystalline materials. This applies, for instance, to metallic nanoparticles where shapes control can improve optical, electrical, and catalytic properties,[1–3] as well as to a large variety of semiconductor structures,[4–6] where the control on morphology allows for the optimization of devices eventually by largely improving the crystalline quality.[7] Moreover, crystal faceting and morphology-dependent properties are of utmost interest for organic compounds used *e.g.* in molecular recognition and in medical applications.[8,9]

The observed crystal shapes are often interpreted in terms of the surface energy minimization which implies the formation of facets corresponding to the minima in the surface energy density function $\gamma = \gamma(\hat{\mathbf{n}})$, where $\hat{\mathbf{n}}$ is the direction of the surface normal. The widely used Wulff construction,[10,11] offers a simple method to determine the equilibrium crystal shape (ECS) with the constraint of a constant volume. This construction is identified as the convex hull of all the planes perpendicular to the $\hat{\mathbf{n}}\gamma(\hat{\mathbf{n}})$ vectors. Several numerical implementations of this procedure are available in literature[12–14] allowing to effectively depict the ECS corresponding to a given $\gamma(\hat{\mathbf{n}})$. Such a description is the most appropriate when considering homogeneous systems very close to the thermodynamic equilibrium while it generally does not hold when considering far-from-equilibrium conditions.[15] If the crystal evolution is fully dominated by kinetics, facet velocities $v(\hat{\mathbf{n}})$ can be considered in place of

$\gamma(\hat{\mathbf{n}})$ and a *kinetic* Wulff construction can still be used in order to predict the final crystal morphology.[16–18] Here we are interested in the intermediate regime where the system tends to minimize free energy but kinetics poses constraints on the actual evolution, and/or the initial morphology brings the system to a local free-energy minimum.

In the seminal work by Mullins in ref 19, a continuum model of surface diffusion, driven by the minimization of the surface energy, was proposed. Methods developed on such basis, including anisotropic $\gamma(\hat{\mathbf{n}})$, widen the range of application of the Wulff approach as they permit to consider the full evolution toward equilibrium giving an explicit description of the intermediate stages.[20,21] The advantage is not simply to provide a time-scale for the evolution but also to account for the influence of the initial geometry, eventually leading to different final configurations despite the same $\gamma(\hat{\mathbf{n}})$ definition. The implementation of versatile surface diffusion simulations with anisotropic surface energy is far from trivial. One of the most relevant difficulty is due to the stiffness of the corresponding partial differential equation (PDE) system. In particular, this becomes critical in the so-called *strong anisotropy* regime, when deep minima are present in $\gamma(\hat{\mathbf{n}})$ such to produce missing orientations and sharp corners in the ECS.[22–24] Another important aspect limiting the model application lies in the representation and tracking of the surfaces. With this respect, Level-Set or Phase-Field (PF) approaches have a substantial advantage thanks to the implicit description of the geometry, allowing to easily manage three dimensional (3D) domains and naturally consider complex topologies eventually changing in time.[21] Several applications of PF methods to the study of anisotropic systems are available in literature (see ref 21 for a review). However, in most cases, only simplified $\gamma(\hat{\mathbf{n}})$ are considered with no claim on describing the complexity of realistic morphologies.

In the present work we introduce a convenient form for $\gamma(\hat{\mathbf{n}})$ and we exploit it within a suitable PF surface diffusion model. The Finite Element Method (FEM) toolbox AMDiS,[29,30] optimized for PF problems, was used. This way, we are able to provide description of the evolution of 3D morphologies with an arbitrary faceting resulting from the choice of $\gamma(\hat{\mathbf{n}})$.

As we shall show, this approach is fully consistent with the standard Wulff approach when considering equilibrium conditions leading to the expected ECS, even in the cases of strong anisotropy. Furthermore, time evolution including major changes in faceting and allowing for a proper description of metastable or out-of-equilibrium states, can be readily tackled.

Model Description

In order to reproduce the surface morphology of 3D geometries and their time evolution, we considered a diffuse-interface approach[21] based on a PF model of surface diffusion including surface energy anisotropy as proposed by Torabi *et al* in ref 25. Within such framework the profile evolution is implicitly tracked by considering an auxiliary analytic function φ, *i.e.* the Phase Field, smoothly varying from $\varphi = 1$ in the solid phase to $\varphi = 0$ in the vacuum. Its expression is given by

$$\varphi = \frac{1}{2}\left[1 - \tanh\left(\frac{3d(\mathbf{r})}{\epsilon}\right)\right], \tag{1}$$

where ϵ is the interface width and $d(\mathbf{r})$ is the signed distance from the (sharp) interface profile (nominally corresponding to the $\varphi = 0.5$ iso-surface) which consists in the surface of the solid phase. Figure 1 shows a spherical shape defined implicitly by means of φ, embedded in a $\varphi = 0$ domain, *i.e.* the vacuum, which is chosen cubic in shape. Every geometrical properties of the surface can be derived directly from φ. In particular the outer surface normal, which defines the local surface orientation, is $\hat{\mathbf{n}} = -\nabla\varphi / |\nabla\varphi|$.

In order to consider an equation for the dynamics of φ, we introduce the surface energy F_s as given by the Ginzburg-Landau energy functional,[21,27]

$$F_{\mathrm{s}}[\varphi] = \int_{\Omega} \gamma(\hat{\mathbf{n}}) \left(\frac{\epsilon}{2}|\nabla\varphi|^2 + \frac{1}{\epsilon}B(\varphi)\right) d\mathbf{r}, \tag{2}$$

with $B(\varphi) = 18\varphi^2 (1-\varphi)^2$, *i.e.* the double well potential which promotes the state $\varphi = 0$ and $\varphi = 1$. According to Onsager linear law, material flow is driven by the gradient of the

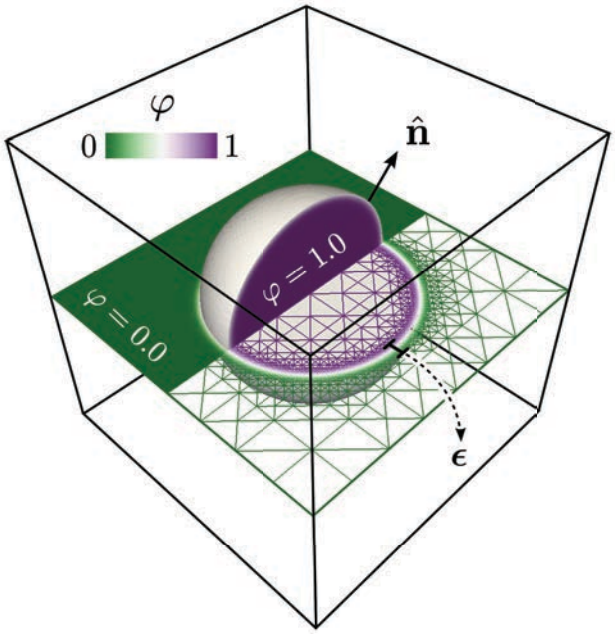

Figure 1: Illustrative scheme of an implicit sphere definition by means of φ. The spherical shape is embedded in the simulation domain consisting in a simple cubic box, whose outline is shown in a perspective view. A slice of the simulation domain reveals its relative size with respect to the sphere, and the refined mesh grid when $\varphi \sim 0.5$.

local chemical potential μ, *i.e.* the variational derivative of eq (2):

$$\begin{aligned} \mu = \mu_{\mathrm{s}} = \frac{\delta F_s}{\delta \varphi} \approx & -\epsilon \nabla \cdot [\gamma(\hat{\mathbf{n}}) \nabla \varphi] + \frac{1}{\epsilon} \gamma(\hat{\mathbf{n}}) B'(\varphi) + \\ & - \epsilon \nabla \cdot \left[|\nabla \varphi|^2 \nabla_{\nabla \varphi} \gamma(\hat{\mathbf{n}}) \right], \end{aligned} \tag{3}$$

where in the last term we used the asymptotic limit $\frac{1}{\epsilon} B(\varphi) \to \frac{\epsilon}{2} |\nabla \varphi|^2$ for $\epsilon \to 0$ and $\nabla_{\nabla \varphi}$ is the gradient which takes effect along the $\nabla \varphi$ direction. This definition of μ corresponds to the well-known Gibbs-Thompson chemical potential.[15] The profile evolution is then defined by tracking the changes of φ according to the continuity law

$$\frac{\partial \varphi}{\partial t} = \nabla \cdot [M(\varphi) \nabla \mu], \tag{4}$$

where the mobility function is set as $M(\varphi) = D \frac{36}{\epsilon} \varphi^2 (1 - \varphi)^2$ to restrict the diffusion at the surface, and D set the timescale of the evolution. The evolution driven by eq (3) is

well-posed only for weak anisotropy regime.

If $\gamma(\mathbf{n})$ is such to give strong anisotropy, the so-called Willmore regularization [25,28] must be included in the free energy definition as an additional term F_{reg}, approximating the integral of the squared local curvature:

$$F_{\mathrm{reg}} = \frac{\beta}{2\epsilon} \int_{\Omega} \left(-\epsilon \nabla^2 \varphi + \frac{1}{\epsilon} B'(\varphi) \right)^2 d\mathbf{r}. \tag{5}$$

Such regularization is a penalizing term which increases the energy of high curvature regions, healing the expected instabilities in the surface diffusion, and its effect on the morphology consists in a rounding of the corners controlled by the β parameter. From a physical point of view this term can also be interpreted as an edge/corner energy. [22] In presence of the regularization, μ must include also a $\delta F_{\mathrm{reg}}/\delta\varphi$ term leading to

$$\mu = \mu_{\mathrm{s}} + \beta \left(-\nabla^2 \kappa + \frac{1}{\epsilon^2} B''(\varphi)\kappa \right), \tag{6}$$

where μ_{s} is given by eq (3) and $\kappa = -\epsilon\nabla^2\varphi + \frac{1}{\epsilon}B'(\varphi)$. Notice that when including the regularization, a 6-th order PDE has to be solved. This is quite demanding from a numerical point of view and accurate space and time discretization are in general required. The FEM toolbox AMDiS [29,30] has been used as it allows to efficiently manage the numerical integration of the reported equations. In fact, space adaptivity is built-in, allowing for a fine spatial resolution at the interface where φ varies significantly and the surface diffusion is active (see Figure 1). This ensures to describe the interface region with a good enough accuracy while coarser resolution is used in the bulk region saving computational cost. Time adaptivity has been also considered to optimize the evolution time steps on the basis of the maximum variation of the profile. Zero-flux Neumann BCs are set at all the domain boundaries (faces of the cubic box in Figure 1). For the sake of simplicity, the unit of length is dimensionless while the timescale is given in $1/(\gamma_0 D)$ units by setting γ_0 and D equal to 1. The details about the integration scheme are reported in the Supporting Information.

Surface-Energy Density: a convenient form

A fully customizable formulation for the $\gamma(\hat{\mathbf{n}})$ function is here introduced in order to arbitrarily tune the equilibrium morphology. The key point for such a function is to quantify the difference between the local surface orientation $\hat{\mathbf{n}}$ and the vectors which give minima in the surface energy density ($\hat{\mathbf{m}}_i$).[31] This is achieved by considering the scalar product $\hat{\mathbf{n}} \cdot \hat{\mathbf{m}}_i$. Then the surface energy can be parametrized as

$$\gamma(\hat{\mathbf{n}}) = \gamma_0 \left(1 - \sum_i^N \alpha_i \left(\hat{\mathbf{n}} \cdot \hat{\mathbf{m}}_i \right)^{d_i} \Theta \left(\mathbf{n} \cdot \mathbf{m}_i \right) \right), \tag{7}$$

where N is the total number of energy minima. α_i and d_i are positive coefficients setting the depth and the width of the minima, respectively. $d_i \geq 2$ for continuity. The Heaviside step function Θ is used in order to exclude energy contributions when the component of $\hat{\mathbf{n}}$ along the $\hat{\mathbf{m}}_i$ direction is negative. This allows us to control $\pm\hat{\mathbf{m}}_i$ facets independently. The role of each term in the summation of eq (7) can be easily inferred by considering how $\gamma(\hat{\mathbf{n}})$ looks in presence of a single minimum $\hat{\mathbf{m}}$. It is equal to $\gamma_0(1-\alpha)$ if $\hat{\mathbf{n}} \equiv \hat{\mathbf{m}}$ and it increases up to γ_0 moving away from $\hat{\mathbf{m}}$. It is worth to mention that our definition leads to some commonly used functions of surface energy density such as $\gamma(\hat{\mathbf{n}}) = \gamma_0 \left[1 + \tilde{\alpha} \left(n_{\mathbf{x}}^4 + n_{\mathbf{y}}^4 + n_{\mathbf{z}}^4 \right) \right]$, reproducing crystal structures with cubic symmetry,[25,26] obtained by considering the six minima along the orthogonal axes $\hat{\mathbf{m}}_{1,2}$=[$\pm$100], $\hat{\mathbf{m}}_{3,4}$=[0$\pm$10], $\hat{\mathbf{m}}_{5,6}$=[00$\pm$1], $d_i = 4$ and constant α_i for each minimum.

In Figure 2(a)-(c) some illustrative 2D surface energy density functions $\gamma(\theta)$ (with $\theta = -\arctan(n_y/n_x)$ the angle between the normal vector and the [10] direction) are reported. In particular, a case with minima at $\bar{\theta}_n = \pm n\pi/4$ with $0 \leq n \leq 4$ (*i.e.* $\langle 10 \rangle$ and $\langle 11 \rangle$ directions) is considered. In Figure 2(a) we show the curves obtained with three different values of d_i but the same α_i. Notice that the width of the energy minima is inversely proportional to d_i. Moreover, when $d_i = 8$, a significant superposition of different contributions in the summation of eq (7) is recognized for all orientations, and $\gamma(\bar{\theta}_n)$ results lower than $\gamma_0(1-\alpha_i)$.

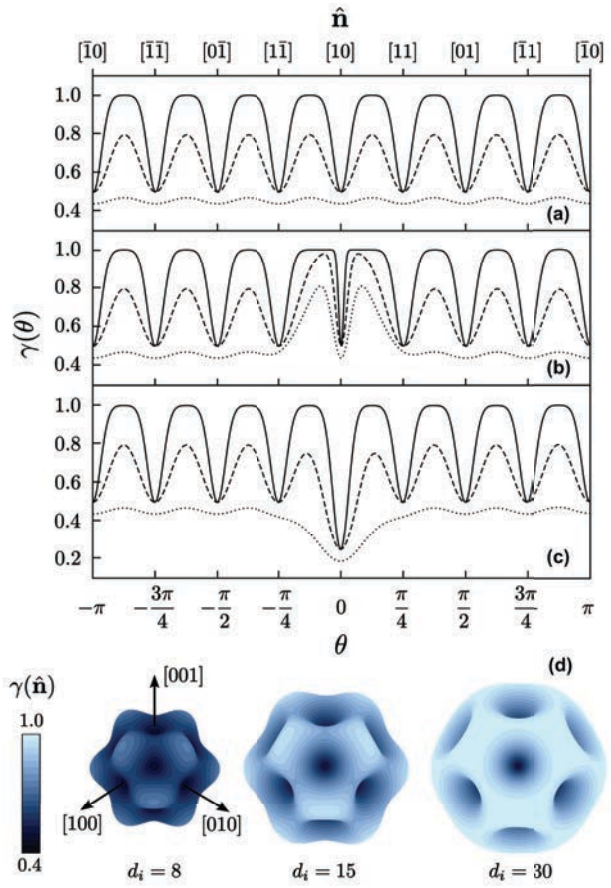

Figure 2: Examples of surface energy density from eq (7). (a)-(c) Plot of 2D $\gamma(\theta)$ function with minima at $\bar{\theta}_n = \pm n\pi/4$ ($\langle 10\rangle$ and $\langle 11\rangle$ directions) with $\alpha_i = 0.5$ and $\gamma_0 = 1$. (a) $d_i = 8$ (dotted line), $d_i = 20$ (dashed line) and $d_i = 100$ (solid line). (b) as in panel (a) with d of $\bar{\theta}_0$) minimum increased by a factor 10. (c) as in panel (a) with $\alpha = 0.75$ for the $\bar{\theta}_0$ minimum. (d) Three-dimensional $\gamma(\hat{\mathbf{n}})$-plot with minima along $\langle 100\rangle$ and $\langle 111\rangle$ directions, $\alpha_i = 0.5$ and $\gamma_0 = 1$, for three d_i values. $\gamma(\hat{\mathbf{n}})$ values are also plotted as surface color map.

Increasing d_i (see $d_i = 20$ curve), no effective superposition is recognized at $\theta = \bar{\theta}_n$ but it still occurs for orientations in between. For large enough d_i (*e.g.* $d_i = 100$), a full decoupling of the energy minima is achieved and orientations with $\gamma(\theta) = \gamma_0$ appear. Features of eq (7) can be also controlled in order to localize a single minimum, as required in order to tune independently the energy value corresponding to the minima orientations, *i.e.* the energy of the facets. This is made clear in Figure 2(b), where the same curves shown in panel (a) are considered with d_i increased by a factor 10 for the $\bar{\theta}_0$ minimum. Furthermore, we can enhance the stability of the $\theta = \bar{\theta}_0$ orientation, by setting a deeper minimum with higher α_i,

as shown in Figure 2(c). Similar arguments hold also when three-dimensional $\gamma(\hat{\mathbf{n}})$ functions are considered. In this case the superposition of the minima contribution can be even more complex, but still the qualitative behavior of the 2D case is recognized. In Figure 2(d), some $\gamma(\hat{\mathbf{n}})$-plots are shown for minima along $\langle 100 \rangle$ and $\langle 111 \rangle$ directions, $\alpha_i = 0.5$ and three different d_i values. The color map reveals the superposition and decoupling effects observed for increasing d_i value. From a general point of view, eq (7) can then be considered as a convenient way to construct a continuum $\gamma(\hat{\mathbf{n}})$ from discrete values corresponding to energy minima.

With an arbitrary choice of eq (7) parameters, $\gamma(\hat{\mathbf{n}})$ can become non-convex, thus requiring the regularization introduced in eq (5). A remarkable analytic criterion has been developed in ref 26 in order to determine if missing orientation occur in the ECS for a given $\gamma(\hat{\mathbf{n}})$. This consists in evaluating when the product of the two gaussian curvatures $K_1 K_2$ of the $1/\gamma$-plot is negative. We used this criterion in order to determine *a priori* what is the expected regime related to the choice of the $\gamma(\hat{\mathbf{n}})$ parameters. For a single minimum direction we evaluated the critical α coefficient as function of the d value, by numerically solving $K_1 K_2 = 0$ condition (see Supporting Information for the explicit formulas). The resulting curve is shown in Figure 3 and it is well reproduced by

$$\alpha_c(d) = \frac{A}{d} + \frac{B}{d^2} \tag{8}$$

where $A = 2.26 \pm 0.2\%$ and $B = -2.48 \pm 0.4\%$ deliver the best fit. If minima contribution in eq (7) are decoupled, one can directly assess what is the anisotropy regime only by comparing the α_i values with the data in Figure 3 or with eq (8). Conversely, if minima contributions are superimposed for some orientation, the explicit numerical evaluation of $K_1 K_2$ is required in order to determine the anisotropy regime and the critical parameters.

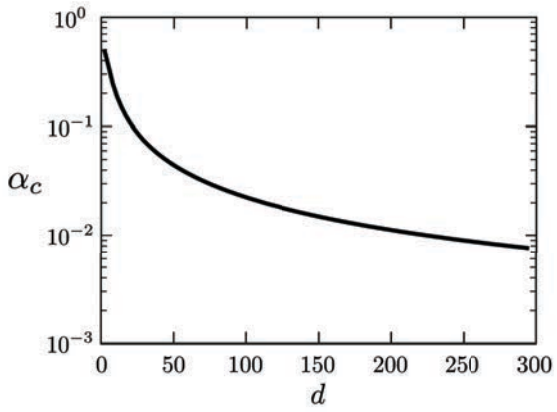

Figure 3: Critical α values as function of d obtained by numerically solving $K_1 K_2 = 0$ for a $\gamma(\hat{\mathbf{n}})$ defined by eq (7) with a single minimum orientation.

Results and Discussion

Evolution from a sphere toward the Equilibrium Crystal Shape

As first case study, we focus on obtaining the ECS as stationary state delivered by surface diffusion simulations via the aforementioned PF model. Furthermore we inspect the customization of the final geometry by suitable choices of the $\gamma(\hat{\mathbf{n}})$ in eq (7), tuning its parameters as well as the strength of the Willmore regularization β. We consider a sphere of radius 0.3 as initial profile, implicitly defined into the integration domain, set as a cubic box with lateral size equal to 1, as shown in Figure 1. The interface width ϵ has been chosen equal to 0.04. The profile evolution is then performed by integrating the surface diffusion equation for φ, letting the geometry free to rearrange into a faceted one according to the $\nabla\mu$.

Figure 4 provides some examples of simulation results obtained starting from a spherical profile and evolving toward equilibrium according to eq (4), for different definitions of $\gamma(\hat{\mathbf{n}})$. In Figure 4(a) we consider the simplest case of $\gamma(\hat{\mathbf{n}})$, where minima directions correspond to the facet orientations of a tetrahedron. As made evident by the evolution sequence, facets are gradually formed from the initial spherical profile leading to the expected polyhedron as equilibrium condition. In Figure 4(b) a different $\gamma(\hat{\mathbf{n}})$ with two different families of

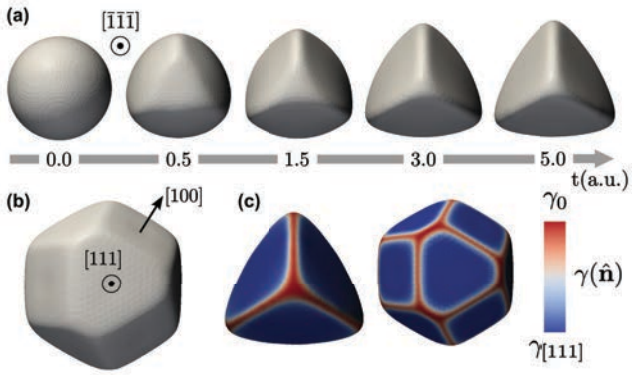

Figure 4: Surface diffusion evolution toward the ECS. (a) From a sphere to a tetrahedron with minima of $\gamma(\hat{\mathbf{n}})$ along $[\bar{1}\bar{1}1]$,$[\bar{1}1\bar{1}]$,$[1\bar{1}\bar{1}]$ and $[111]$ directions with $\alpha_i = 1.0$, $d_i = 6$, $\beta = 0.002$. (b) ECS simulated by considering minima along $\langle 100\rangle$ and $\langle 111\rangle$ directions with $\alpha_i = 0.3$, $d_i = 20$ and $\beta = 0.001$. (c) Color map, scaled by the $\gamma_{[111]}$ value, showing the $\gamma(\hat{\mathbf{n}})$ for the geometries shown in (a) and (b), respectively.

minima directions, along $\langle 100\rangle$ and $\langle 111\rangle$, is considered, and the resulting ECS is shown. In Figure 4(c) the actual faceting of the final geometries reported in Figures 4(a) and 4(b) is made more clear by showing $\gamma(\hat{\mathbf{n}})$ as a color map at the surface. The large regions in uniform (blue) color correspond to almost flat facets oriented according to the minima in $\gamma(\hat{\mathbf{n}})$, while edges and corners in between have higher energy as they smoothly connect facets with intermediate orientations with respect to the minimum energy ones.

By tuning the parameters of eq (7) we can modify also the features of the equilibrium shape for a given set of minimum directions. Figure 5(a) shows the ECS obtained with the same $\gamma(\hat{\mathbf{n}})$ used in Figure 4(b) with different anisotropy degrees, *i.e.* with different α_i values. Both weak and strong anisotropy are considered. Notice that, even for weak anisotropy, preferential orientations are present but with rather large angular dispersion around minima so that an almost rounded geometry is still obtained. The selectivity on the minima orientation increases for larger α_i leading to more defined facets. As a result, the stronger is the anisotropy the more contracted are the (red) areas with high $\gamma(\hat{\mathbf{n}})$ between the facets. It must be noticed that, due to the requirements of continuous profile, such rounded edges/corners cannot be avoided. Polyhedron-like structures can then be obtained only by restricting such region as much as possible by increasing α. However, when entering

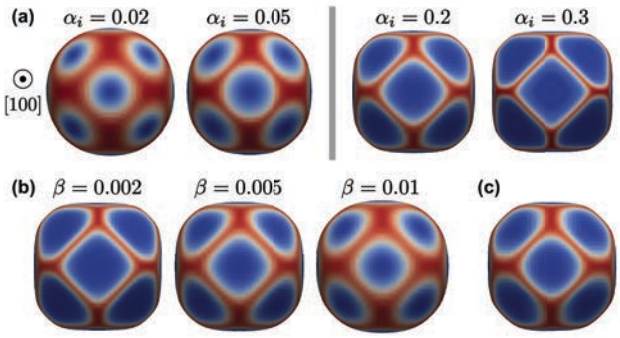

Figure 5: Dependance of ECS on: (a) α_i, both in weak (left) and strong (right) anisotropy regime, (b) β values, (c) the radius of the initial sphere, here considered doubled with respect to the one in panel (e) with $\beta = 0.01$. Minimum directions are set as in Figure 4(b). $\gamma(\hat{\mathbf{n}})$ color map is shown as in Figure 4(c).

in the strong anisotropy regime, the Willmore regularization term introduces an additional driving force toward rounding, depending on the parameter β. In Figure 5(b), the same $\gamma(\hat{\mathbf{n}})$ used in Figure 4(b), has been considered with different β values. We notice that the larger is its value the more extended is the rounded area between the different facets.[22,25] Furthermore, the effect is more dramatic at the corners than at the edges, as the local curvature is larger. In order to obtain sharper facets, for a given set of $\gamma(\hat{\mathbf{n}})$ parameters, one should then lower β as much as possible. However, the lowest values which can be used for such a parameter depends in general on the interface width and on the spatial discretization of the FEM method. All these simulation features should be chosen as a trade-off between the need to obtain sharp facets and the computational costs. It must be also pointed out that, at variance from the $\gamma(\hat{\mathbf{n}})$ contribution which produces self-similar geometries when rescaling the crystal volume, the Willmore regularization is set on an absolute length scale since β directly defines the rounding radius, independently on the facets extension.[25] This is illustrated in Figure 5(c) where the radius of the crystal is doubled, while keeping the same $\gamma(\hat{\mathbf{n}})$ used in Figure 5(b) (with $\beta = 0.01$). The relative extensions of the rounded regions at the edges are more localized, thus the shape looks more similar to the case with lower β values, *i.e.* sharper facets are obtained.

More complex geometries can also be reproduced since our definition of $\gamma(\hat{\mathbf{n}})$ does not rely

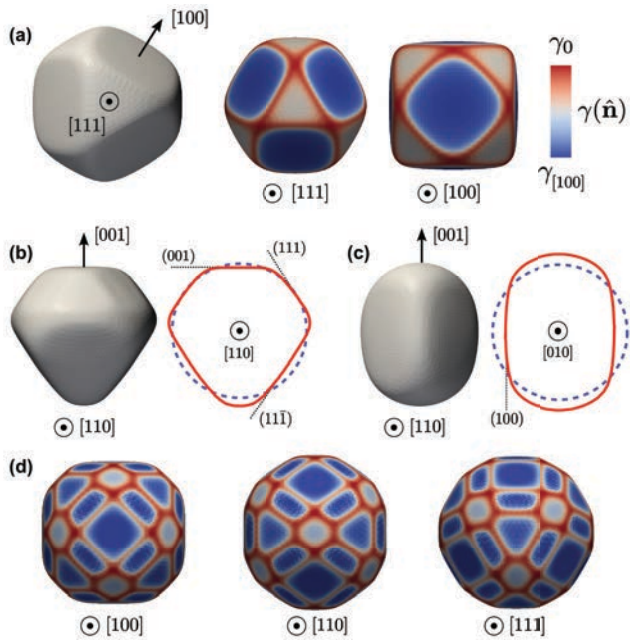

Figure 6: ECSs obtained by arbitrary tuning of the $\gamma(\hat{\mathbf{n}})$. (a) As in Figure 4(b) with halved value of α_i along $\langle 111 \rangle$ directions. Perpective 3D view and $\gamma(\hat{\mathbf{n}})$ color map are shown. In (b) and (c) we show asymmetric shape with perspective 3D views and with comparisons in a central cross-section between the resulting shape and the initial spherical profile. Parameters in (b): [001], [$\pm$1$\pm$11], [$\pm$101], [0$\pm$11] minima directions with $\alpha_i = 0.2$ and $d_i = 60$, [$\pm$1$\pm$1$\bar{1}$] minima directions with $\alpha_i = 0.4$ and $d_i = 30$. $\beta = 0.002$. Parameters in (c): minima along [$\pm$100] and [0$\pm$10] with $\alpha_i = 0.4$, $d_i = 10$, $\beta = 0.002$). (d) Shape of a Ge crystal including {001}, {110}, {111} and {113} facets by considering energy minima as in ref 32 with $\beta = 0.003$, $d_i = 100$ for minima along {113} directions and $d_i = 50$ for the others, $\alpha_{\{001\}} = 0.3$.

on any imposed symmetry in the surface energy, as shown with few examples in Figure 6. In particular, Figure 6(a) illustrates the effect of setting different energy values for the minima in $\gamma(\hat{\mathbf{n}})$. The same parameters of Figure 4(b) are considered but α_i corresponding to the minima along $\langle 111 \rangle$ directions are lowered by a factor 2. As expected, the resulting ECS exhibits much larger [100] facets, thanks to their enhanced stability. Examples of more complex, asymmetric ECS are shown in Figures 6(b) and 6(c). From the reported results we conclude that within our PF approach we can control the ECS features, eventually matching the standard Wulff construction in the limit $\beta \to 0$.

This makes our method suitable to investigate realistic systems which exhibit ECS-like structures, such as those shown in refs 1–3 (where some morphologies recall the ones ob-

tained so far). An example where we reproduce a specific realistic morphology is illustrated in Figure 6(d), where theoretical data for Ge surface energy[32] are used to set $\gamma(\hat{\mathbf{n}})$ and predict the corresponding ECS. Furthermore, another important application could consists in matching simulated ECS with experimental shapes in order to obtain estimates of $\gamma(\hat{\mathbf{n}})$.

Morphologies of long-lived, metastable structures

The ECS can be in general considered as the ideal state toward which a system should tend. However, the outcome of experiments may not correspond to it because of the presence of sufficiently long-lived metastable, or kinetically frozen out-of-equilibrium states. Importantly, present nanoscience and nanotechnology widely exploits structures which do not correspond to a global minimum in the phase-space (quantum dots or nanowires being only two possible examples), as they can display a peculiar behavior, absent in the lowest free-energy state. Faceting of morphologies not corresponding to global equilibrium can be described by suitable cutting of the ECS or by specific modifications in the Wulff construction procedure,[13,33] but care is needed in extracting actual details of $\gamma(\hat{\mathbf{n}})$ by a simple comparison between model and experiments, particularly when one is willing to account for the temporal evolution of a faceted crystal.

A more appropriate description should be based on a unique definition of $\gamma(\hat{\mathbf{n}})$ from experimental data of systems at equilibrium (or from theoretical calculations as in Figure 6(d)). Deviations from the ECS could then be explained by considering the initial out-of-equilibrium geometry and taking into account the time evolution of the profile, driven by its tendency to the equilibrium. Our approach allows to tackle this additional degree of complexity as it does not consist in a simple minimization of the surface energy but provides the whole evolution path toward it. In the following we present some examples of nanostructure morphologies, reproduced by setting $\gamma(\hat{\mathbf{n}})$ from data in literature and considering suitable initial profiles.

Homoepitaxial islands[34] or top-down designed patterns produced by lithography[35] fall in the description discussed above as their shape can be substantially different from the

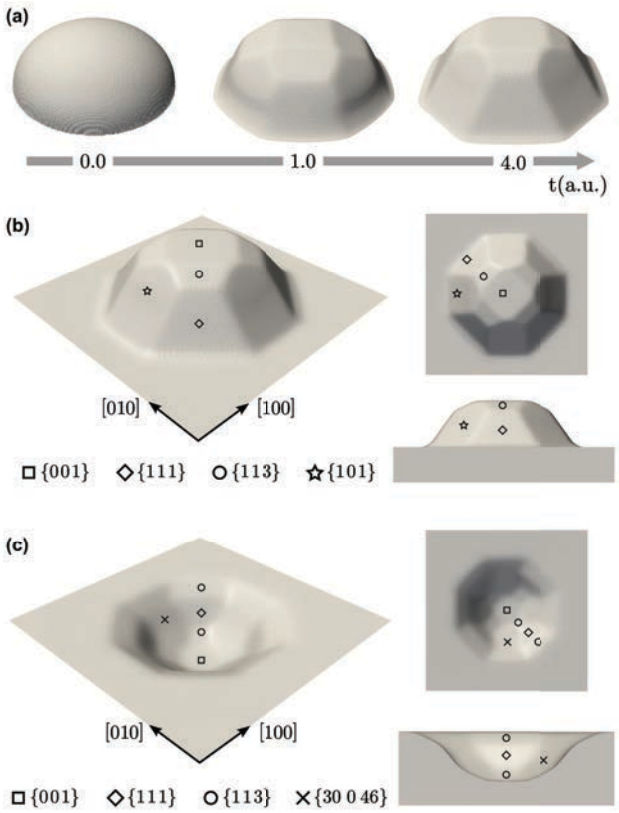

Figure 7: Faceting of structures on surfaces. (a) Evolution from the initial configuration by including [001],[±1±11],[±1±13],[±101] and [0±11] facets,[36,37] $\alpha_i = 0.035$, $\beta = 0.002$. d_i are set as in Figure 6(d). (b) Detailed view of the $t = 4.0$ stage of the evolution in panel (a) revealing an island faceting similar to the one obtained with GaAs in ref 34. (c) Faceting reproducing the one occurring in Si pit-patterned substrates as in ref 35 obtained by imposing minima at [001], [±1±11], [±1±13], [±30 0 46] and [0 ±30 46] directions,[32] $\alpha_i = 0.03$, $\beta = 0.003$. d_i are set as in Figure 6(d) and $d_{\{30\ 0\ 46\}} = 100$.

equilibrium configuration according to the specific fabrication processing. For the sake of simplicity we set minimum energy directions in $\gamma(\hat{\mathbf{n}})$ and assume the same α_i (large enough to obtain sharp facets). Figure 7 shows simulations reproducing the morphology of an island (in panels (a) and (b)) and of a pit-patterned substrate (in panel (c)). Here the interface thickness is set equal to 0.1. More precisely, the island morphology was obtained starting from an half ellipsoidal shape intersecting a plane below which $\varphi = 1$ (for half of the cubic domain) as shown in Figure 7(a) for $t = 0.0$, with an height-to-base aspect-ratio of 0.35 (in agreement with experimental ones[34]), and a lateral size equal to 2.4. The surface energy minima orientations are set according to theoretical data for GaAs.[36,37] The

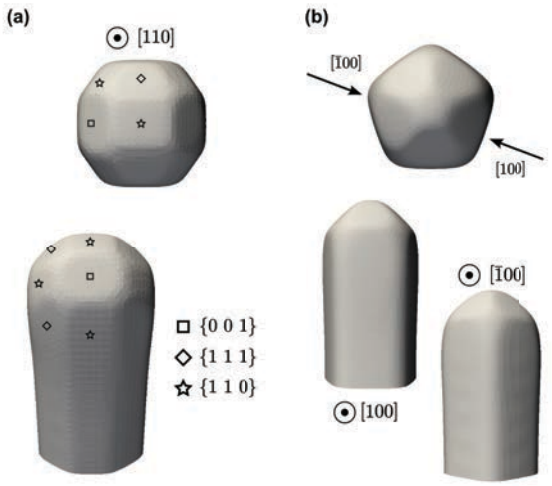

Figure 8: Morphology of far-from-equilibrium elongated shapes. (a) [110] Ge nanowire morphology including {100}, {110} and {111} as in ref 5, obtained by selecting minima energy ratio of the Ge crystal[32] and $\alpha_{[001]} = 0.15$. (b) Ag nanowire with pentagonal symmetry[39] obtained by considering $\gamma(\hat{\mathbf{n}})$ in an effective way with minima along [sin($2n\pi/5$) cos($2n\pi/5$) 0] and [sin($2n\pi/5$) cos($2n\pi/5$) 1] directions with $0 \leq n \leq 4$, $\alpha_i = 0.15$, $d_i = 30$, $\beta = 0.002$.

evolution of such initial configuration, reported in Figure 7(a), shows different faceted island structures resulting from different stages of the surface diffusion evolution. Notice that all these structures correspond to metastable configuration, as the final state would be the flat surface. The shape obtained at $t = 4.0$, characterized in Figure 7(b), closely matches the morphology of GaAs nanometric islands observed in experiments, as in ref 34. The simulation of a pit geometry illustrated in Figure 7(c) has been obtained by considering as initial profile a pit with a flat (001) surface at the bottom and a smooth connection with the surrounding flat substrate. The pit aspect-ratio is set to 0.3, to reproduce a typical pit morphology resulting from etching,[38] with a lateral size of 2. The $\gamma(\hat{\mathbf{n}})$ minima orientations are set to reproduce the Si minimum energy surfaces.[32] $\langle 30\ 0\ 46 \rangle$ minima directions are considered in order to mimic neighboring $\langle 15\ 3\ 23 \rangle$ facets (*e.g.* [15 $\pm$3 23]) recognized in experiments. Also in this case the resulting morphology closely resembles the experimental morphology of pit-patterned Si(001) substrate reported in literature.[35,38]

Low-dimensional systems and elongated shapes can be considered as well as non-equilibrium structures as their structures result from the growth mechanisms and are not due to extreme

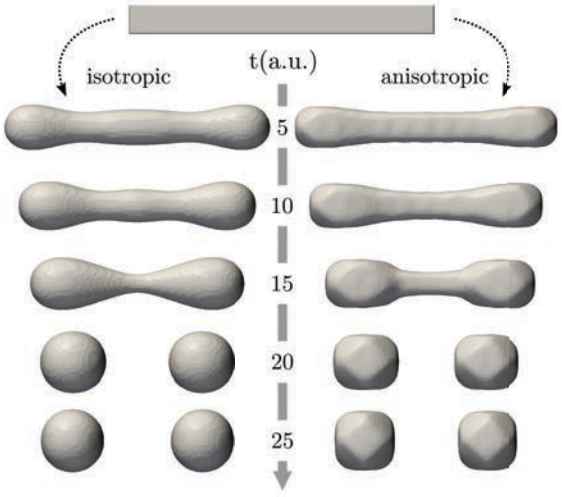

Figure 9: Surface diffusion evolution of a parallelepiped shape with of isotropic (left) and anisotropic (right) $\gamma(\hat{\mathbf{n}})$, the latter as in Figure 5(a) with $\alpha_i = 0.2$.

differences in their $\gamma(\hat{\mathbf{n}})$ minima. Also in these cases, our modeling is effective to describe the main morphological features and the temporal evolution of facets. Examples are shown in Figure 8 where realistic nanowires are reproduced by means of surface diffusion evolution starting from a simplified parallelepiped shape, placed with the base in contact with the domain boundary to mimic the continuation of the lateral facets. In Figure 8(a) the morphology of a Ge nanowire grown along [110] direction is reproduced, closely resembling the experimental structures as shown for instance in ref 5, including both top and sidewalls faceting. $\gamma(\hat{\mathbf{n}})$ values were selected according to the data reported in ref 32 for the energy minima along {100}, {110} and {111} directions. Another example is provided in Figure 8(b), where the morphology of an Ag nanowire with pentagonal symmetry, reported in ref 39, is well matched by simulations. Notice that this peculiar morphology results from twinning of five single crystal subunits exposing only {111} facets, so that the selected five-fold $\gamma(\hat{\mathbf{n}})$ minima are not meant to reproduce the anisotropy of a single Ag crystal, but include the rotation around the nanowire axis of each subunit.

So far we considered systems where the evolution dynamics consisted only in a rearrangement of facets. Different initial conditions can however lead to more dramatic effects

changing the topology of the system. This is shown by illustrative simulations in Figure 9 where the evolution of an initial high aspect-ratio paralleleliped, completely embedded in the $\varphi = 0$ phase, is considered. Surface diffusion induces a strong recalling of material toward the borders up to the separation of the initial profile in two distinct crystals, an outcome which is clearly far from the ECS. This is found to occur for both isotropic and anisotropic surface energy density (in the latter case $\gamma(\hat{\mathbf{n}})$ is set as in Figure 5(a) with $\alpha_i = 0.2$). Notice that such a dynamics is naturally included in the PF description[21] thus representing a neat advantage over other methods, allowing to simulate topological changes also in the case of highly anisotropic surface energy density. This enables the study of physical systems showing similar behavior, as for instance solid-state dewetting phenomena,[40–42] including a fine description of surface morphology.

Conclusions

In this work we have introduced a convenient definition of orientation-dependent surface energy which, when accompanied by a proper regularization term and implemented within a suitable PF framework, allows one to obtain arbitrary faceted shapes by surface diffusion. If no free-energy barriers are present, our approach leads, for long-enough evolution times, to the ECS corresponding to the Wullf construction. However, the main advantage stems in the possibility of describing faceting on out-of-equilibrium shapes, resulting in their time-dependent morphological evolution, eventually leading to a local free-energy, metastable minimum. Applications to relevant metastable nanostructures such as nanowires or dots were illustrated, revealing several features observed in experiments and pointing out the importance of the initial configuration in determining the observed facets extension in long-lived metastable states.

Importantly, the here provided methodology can be extended to other PF models tackling additional energy contributions affecting the profile evolution, such as elasticity,[44] intermix-

ing effects for alloys and multi-component systems,[45] as well as peculiar boundary conditions, *e.g.* contact angles at the interface of two materials.[46] Inclusion of such further phenomena would result in an unprecedented ability in modeling the time-evolution of complex nanostructures.

Acknowledgement

The strong need for a realistic model able to tackle faceting of metastable structures was first pointed out to us by Prof Leo Miglio. This work was partially supported by the Cariplo Foundation (DEFCON-IV project). R.B. and A.V. acknowledge support from the German Science Foundation within SPP 1296 Vo899/7 and EXC CfAED as well as the European Commission within FP7-PEOPLE-2009-IRSES PHASEFIELD. Simulations were carried out at ZIH at TU Dresden and JSC at FZ Jülich.

Supporting Information Available

Details about the anisotropy regime assessment and the explicit integration scheme adopted in the PF simulations. This material is available free of charge via the Internet at `http://pubs.acs.org/`.

References

(1) Sun Y. G.; Xia Y. N. Shape-Controlled Synthesis of Gold and Silver Nanoparticles. *Science* **2002**, *298*, 2176–2179.

(2) Tao A. R.; Habas S.; Yang P. Shape Control of Colloidal Metal Nanocrystals. *Small* **2008**, *4*, 310–325.

(3) Barnard A. S.; Young N. P.; Kirkland A. I.; van Huis M. A.; Xu H. Nanogold: A Quantitative Phase Map. *ACS Nano* **2009**, *3*, 1431–1436.

(4) Medeiros-Ribeiro G.; Bratkovski A. M.; Kamins T. I.; Ohlberg D. A. A.; Williams R. S. Shape Transition of Germanium Nanocrystals on a Silicon (001) Surface from Pyramids to Domes. *Science* **1998**, *279*, 353–355.

(5) Hanrath T.; Korgel B. A. Crystallography and Surface Faceting of Germanium Nanowires. *Small* **2005**, *1*, 717–721.

(6) Falub C. V.; von Känel H.; Isa F.; Bergamaschini R.; Marzegalli A.; Chrastina D.; Isella G.; Müller E.; Niedermann P.; Miglio L. Scaling Hetero-Epitaxy from Layers to Three-Dimensional Crystals. *Science* **2012**, *335*, 1330–1334.

(7) Bergamaschini R.; Isa F.; Falub C. V.; Niedermann P.; Müller E.; Isella G.; von Känel H.; Miglio L. Self-Aligned Ge and SiGe Three-Dimensional Epitaxy on Dense Si Pillar Arrays. *Surf. Sci. Rep.* **2013**, *68*, 390–417.

(8) An Q.; Dong C.; Zhu W.; Tao C.; Yang H.; Wang Y.; Li G. Cucurbit[8]uril as Building Block for Facile Fabrication of Well-Defined Organic Crystalline Nano-objects with Multiple Morphologies and Compositions. *Small* **2012**, *8*, 562–568.

(9) Auyeung E.; Li T. I. N. G.; Senesi A. J.; Schmucker A. L.; Pals B. C.; Olvera de la Cruz M.; Mirkin C. A. DNA-Mediated Nanoparticle Crystallization into Wulff Polyhedra. *Nature* **2014**, *505*, 73–77.

(10) Wulff, G. On the Question of the Rate of Growth and Dissolution of Crystal Surfaces. *Z. Kristallogr.* **1901**, *34*, 449–530.

(11) Herring C. Some Theorems on the Free Energies of Crystal Surfaces. *Phys. Rev.* **1951**, *82*, 87–93.

(12) Roosen A. R.; McCormack R. P.; Carter W. C. Wulffman: A Tool for the Calculation and Display of Crystal Shapes. *Comput. Mater. Sci.* **1998**, *11*, 16–26.

(13) Zucker R. V.; Chatain D.; Dahmen U.; Hagege S.; Carter W. C. New Software Tools for the Calculation and display of Isolated and Attached Interfacial-Energy Minimizing Particle Shapes. *J. Mater. Sci.* **2012**, *47*, 8290–8302.

(14) Scopece D. SOWOS: an Open-Source Program for the Three-Dimensional Wulff Construction. *J. Appl. Cryst.* **2013**, *46*, 811–816.

(15) Pimpinelli A.; Villain J., *Physics of Crystal Growth*, Cambridge University Press, 1998.

(16) Frank F. C. On the Kinematic Theory of Crystal Growth and Dissolution Processes. In *Growth and Perfection in Crystals*, Doremus R. H., Roberts B. W., Turnbull D., Eds.; John Wiley & Sons Inc.: New York, 1958.

(17) Chernov A. A. The Kinetics of the Growth Forms of Crystals. *Sovi. Phys. Crystallogr.* **1963**, *7*, 728–730.

(18) Shaw W. Morphology Analysis in Localized Crystal Growth and Dissolution. *J. Cryst. Growth* **1979**, *47*, 509–517.

(19) Mullins W. W. Theory of Thermal Grooving. *J. Appl. Phys.* **1957**, *28*, 333–339.

(20) Carter W. C.; Roosen A. R.; Cahn J. W.; Taylor J. E. Shape Evolution by Surface Diffusion and Surface Attachment Limited Kinetics on Completely Faceted Surfaces. *Acta Metall. et Mater.* **1995**, *43*, 4309–4323

(21) Li B.; Lowengrub J.; Ratz A. and Voigt A. Geometric Evolution Laws for Thin Crystalline Films: Modeling and Numerics. *Commun. Comput. Phys.* **2009**, *6*, 433–482.

(22) Spencer B. J. Asymptotic Solutions For the Equilibrium Crystal Shape with Small Corner Energy Regularization. *Phys. Rev. E* **2004**, *69*, 011603.

(23) Eggleston J. J.; McFadden G. B. and Voorhees P. W. A Phase-Field Model for Highly Anisotropic Interfacial Energy. *Physica D* **2001**, *150*, 91–103.

(24) Gurtin M., *Thermodynamics of Evolving Phase Boundaries in the Plane*, Oxford University Press, 1993.

(25) Torabi S.; Lowengrub J.; Voigt A. and Wise S. A New Phase-Field Model for Strongly Anisotropic Systems. *Proc. R. Soc. A* **2009**, *465*, 1337–1359.

(26) Sekerka, R. F. Analytical Criteria for Missing Orientations On Three-Dimensional Equilibrium Shapes. *J. Cryst. Growh* **2005**, *275*, 77–82.

(27) Cahn J.W.; Hilliard J. E. Free Energy of a Nonuniform System. I. Interfacial Free Energy. *J. Chem. Phys* **1958**, *28*, 258–267.

(28) Du Q.; Liu C.; Ryham R.; Wang X. A Phase Field Formulation of the Willmore Problem. *Nonlinearity* **2005**, *18*, 1249–1267.

(29) Vey S.; Voigt A. AMDiS: Adaptive Multidimensional Simulations. *Comput. Visual. Sci.* **2007**, *10*, 57–67.

(30) Witkowski T.; Ling S.; Praetorius S.; Voigt A. Software concepts and numerical algorithms for a scalable adaptive parallel finite element method. *Adv. Comput. Math.* **2015**, In Press. DOI:10.1007/s10444-015-9405-4.

(31) Siem E. J.; Carter W. C. Orientation-Dependent Surface Tension Functions for Surface Energy Minimizing Calculations. *J. Mater. Sci* **2005**, *40*, 3107–3113.

(32) Stekolnikov A. A.; Bechstedt F. Shape of Free and Constrained Group-IV Crystallites: Influence of Surface Energies. *Phys. Rev. B* **2005**, *72*, 125326.

(33) Winterbottom W. L. Equilibrium Shape of a Small Particle in Contact with a Foreign Substrate. *Acta Metall.* **1967**, *15*, 303–310.

(34) Wong P. S.; Liang B. L.; Moleke R.; Tatebayashi J.; Huffaker D. L. Controlled Formation and Dynamic Wulff Simulation of Equilibrium Crystal Shapes of GaAs Pyramidal Structures on Nanopatterned Substrates. *Cryst. Growth Des.* **2010**, *10*, 2509–2014.

(35) Zhang J.J.; Stoffel M.; Rastelli A.; Schmidt O. G.; Jovanovic V.; Nanver L. K.; Bauer G. SiGe Growth on Patterned Si(001) Substrates: Surface Evolution and Evidence of Modified Island Coarsening. *Appl. Phys. Lett* **2007**, *91*, 173115.

(36) Moll N.; Kley A.; Pehlke E.; Scheffler M. GaAs Equilibrium Crystal Shape from First Principles. *Phys. Rev. B.* **1996**, *54*, 8844–8855.

(37) Platen J.; Kley A.; Setzer C.; Jacobi K.; Ruggerone P.; Scheffler M. The Importance of High-Index Surfaces for the Morphology of GaAs Quantum Dots. *J. Appl. Phys.* **1999**, *85*, 3597–3601.

(38) Bergamaschini R.; Tersoff J.; Tu Y.; Zhang J. J.; Bauer G.; Montalenti F. Anomalous Smoothing Preceding Island Formation During Growth on Patterned Substrates. *Phys. Rev . Lett.* **2012**, *109*, 156101.

(39) Wiley B.; Sun Y.; Mayers B.; Xia Y. Shape-Controlled Synthesis of Metal Nanostructures: The Case of Silver. *Chem. Eur. J.* **2005**, *11*, 454–463.

(40) Santala M. K.; Glaeser A. M. Rayleigh instabilities in crystalline solids: Evolution of Finite-Aspect-Ratio Pore Channels in Sapphire. *Acta Mater.* **2008**, *56*, 1967–1980.

(41) Capellini G.; Ciasca G.; De Seta M.; Notargiacomo A.; Evangelisti F.; Nardone M. Agglomeration Process in Thin Silicon-, Strained Silicon-, and Silicon Germanium-on-Insulator Substrates. *J. Appl. Phys.* **2009**, *105*, 093525.

(42) Ye J.; Thompson C.V. Templated Solid-State Dewetting to Controllably Produce Complex Patterns. *Adv. Mater.* **2011**, *23*, 1567–1571.

(43) Karma A.; Rappel W. J. Quantitative phase-field modeling of dendritic growth in two and three dimensions. *Phys. Rev. E* **1998**, *57*, 4323–4349.

(44) Rätz A.; Ribalta A.; Voigt A. Surface Evolution of Elastically Stressed Films Under Deposition by a Diffuse Interface Model. *J. Comput. Phys.* **2006**, *214*, 187–208.

(45) Backofen R.; Bergamaschini R.; Voigt A. The Interplay of Morphological and Compositional Evolution in Crystal Growth: a Phase-Field Model. *Phil. Mag.* **2014**, *94*, 2162–2169.

(46) Jiang W.; Bao W.; Thompson C.V.; Srolovitz D. J. Phase Field Approach for Simulating Solid-State Dewetting Problems. *Acta Mater.* **2012**, *60*, 5578–5592.

Graphical TOC Entry

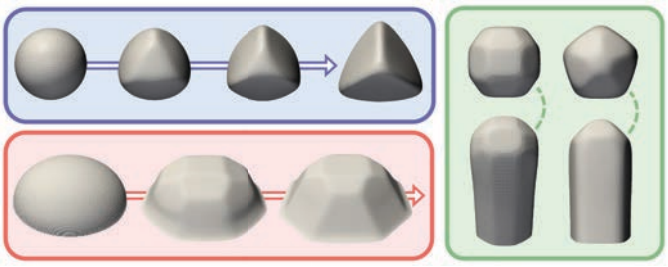

Crystal Morphologies by Phase Field model of surface diffusion